Masters Thesis

Máster en Astrofísica

Vortices in the solar atmosphere

supervised by: Tobías Felipe García

cosupervised by: Elena Khomenko Shchukina

submitted on: Febrero-2022

submitted by: Guillem Castelló i Barceló
alu0101162256@ull.edu.es

Resumen en Español

La atmósfera solar es un medio altamente dinámico compuesto de plasma, gas cargado y de alta temperatura, y campos magnéticos en constante movimiento. El movimiento del plasma y su interacción con el campo magnético subyacente da lugar a toda clase de fenómenos hidrodinámicos, magnéticos y magnetohidrodinámicos.
Uno de los fenómenos solares que más atención ha recibido en los últimos años son los vórtices presentes en la atmósfera solar. Los vórtices son regiones donde el plasma rota respecto a un eje. Son prometedores medios de transporte de materia y energía desde el interior solar hasta las capas más altas de la atmósfera. Además, su estudio es relevante para entender el almacenamiento y liberación de energía magnética y la generación de eventos de reconexión magnética.
A pesar de los avances recientes fruto de este gran interés, el estudio de la vorticidad en la atmósfera solar es todavía una zona activa de investigación con numerosas preguntas abiertas. Una mejor comprensión de la vorticidad y su papel en la atmósfera solar ayudará a obtener una comprensión más profunda de los procesos y fenómenos subyacentes que forman el Sol e impulsan el clima espacial.

En este trabajo nos centraremos en el estudio de vórtices en la atmósfera solar por medio de simulaciones numéricas realistas. En concreto, se emplearon dos series temporales que difieren en la configuración de campo magnético inicial. En ambas simulaciones se identificó la presencia de vórtices mediante diferentes criterios, incluyendo el "swirling strength" y su versión mejorada "Enhanced swirling strength". Este método consiste en la obtención de un parámetro escalar λ (swirling strength) a partir del análisis de autovalores y autovectores del tensor gradiente de velocidades en cada punto de la caja simulada. Posteriormente se aplicarán una serie de filtros para descartar regiones transitorias, de tamaño muy reducido o que rotan muy lentamente.

Al tener identificados todos los vórtices en las distintas series temporales, se llevaron a cabo distintos análisis estadísticos para el estudio de las propiedades de estos y el rol que juegan en el transporte de energía en la atmósfera solar:

- Propiedades de los vórtices: Distribución de volúmenes (en píxeles) de los vórtices. También se comprobó la naturaleza de los vórtices a través del estudio de la ecuación de vorticidad y sus distintos términos.
- Propiedades del plasma: Se estudió cómo varían las propiedades del plasma en zonas donde se han identificado vórtices en comparación con las propiedades medias del plasma. En concreto nos centramos en la densidad de energía cinética.
- Vector de Poynting: Se estudió la estructura del vector de Poynting vertical para comprobar si las regiones con vórtices son zonas de propagación de energía magnética de las capas bajas a las capas altas de la atmósfera solar.
- Relación entre vórtices y temperatura: Finalmente, se han hecho histogramas 2D (Temperatura - Swirling strength) para comprabar si hay correlaciones directas entre la temperatura y la velocidad de rotación de los vórtices a distintas capas de la atmósfera solar.

Hemos comprobado que las regiones identificadas como vórtices presentan distintas características según la capa de la atmósfera solar en la que se encuentren y según la configuración magnética inicial. En interior solar, donde gobierna la convección, la mayoría de los vórtices presentan una estructura irregular y un tamaño pequeño, debido a que estos se forman principalmente por efectos puramente hidrodinámicos. En la fotosfera vemos un descenso importante en el número de vórtices identificados. Debido a las condiciones físicas del medio, y que la convección deja de gobernar, las zonas que se identifican como vórtices son principalmente los extremos de vórtices grandes que conectan la fotosfera con la cromosfera. En la cromosfera hemos visto que la configuración de campo inicial afecta mucho a la forma y tamaño de los vórtices. En los modelos donde inicialmente se impone un campo magnético vertical, los vórtices toman forma alargada casi puramente vertical, envolviendo los tubos de flujo magnético. En cambio, en los modelos donde el campo es generado por dinamo local y es más caótico, las formas son más irregulares y los tamaños más diversos.

Seguidamente, hemos evaluado la contribución de los vórtices al transporte de energía. Para ello, se ha cuantificado la densidad de energía cinética y la componente vertical del vector de Poynting para diferentes alturas del interior y la atmósfera solar. Hemos comparado estas magnitudes en las regiones identificadas como vórtices y las regiones fuera de los vórtices. Nuestros resultados indican que generalmente ambas variables son mayores en los vórtices que fuera de ellos, confirmando la hipótesis de que son estructuras óptimas para el transporte de energía en la atmósfera solar.
Finalmente, se ha estudiado la contribución de los vórtices al calentamiento de la atmósfera solar. Se ha evaluado la correlación entre temperatura y "swirling strength". Hemos visto que la correlación entre estas variables cambia según la capa en la que nos encontremos. En el interior solar, hemos comprobado que no hay una correlación evidente entre ambas magnitudes. En la fotosfera, las regiones con mayor temperatura están producidas casi exclusivamente por regiones con baja "swirling strength". En cambio, en la cromosfera vemos que las regiones con mayor "swirling strength" presentan temperaturas altas. Especulamos que estas correlaciones se deben al transporte de energía desde la fotosfera hasta la cromosfera en los vórtices.

Contents

Chapter 1

Introduction

The study of vorticity in the solar atmosphere has garnered attention in recent years in the Solar Physics community. This boost in the study of solar vortex motions at multiple scales is driven by two complementary approaches. First, the acquisition of high-resolution and high-cadence observations from novel solar instrumentation. Second, the development of state-of-the-art numerical simulations, which allow the study of vortices at scales beyond the observational limits.

They key differences between these methods is the amount of information one has on the plasma motions. While in simulations we have complete knowledge of the physical conditions of the plasma, in observations one must derive most of them for sensible studies in vorticity and also different types of errors must be taken into account, making the labour much more difficult.

1.1 Observations of vortices

With the advances in technology, high-resolution and high-cadence observations are possible and have been made. These improvements allowed the solar physics community to resolve and see vortex-like structures and flows. These structures are generally related to the underlying magnetic field structure. For the different layers of the solar atmosphere different observational techniques were developed.

At photospheric heights, many observational studies are based on tracking and monitoring the evolution of passively advected tracers, such as magnetic bright points. The first observations of vortices in the photosphere were made by Brandt et al. (1988), who reported vortices located at supergranular boundaries. Subsequent works detected convectively-driven vortex flows at smaller scales within intergranular lanes using the movement of bright points (Bonet et al., 2008). This method was later improved through the visual inspection of magnetograms in Bonet et al. (2010). Figure 1.1 shows the results from Bonet et al. (2008), where different sets of magnetic bright points rotate with respect to each other.

The first swirling motions at the solar chromosphere were reported by Wedemeyer-Böhm & Rouppe van der Voort (2009). They employed observations acquired with the CRisp Imaging Spectropolarimeter (CRISP) of the Swedish Solar Telescope (SST) to detect what they called "chromospheric swirls". The nature of these chromospheric swirls was deeply investigated by Wedemeyer-Böhm et al. (2012). They found that the magnetic field concentrated in intergranular lanes, in constant movement due to the action of the granular velocity field and the photospheric oscillations, can create a coherent, almost vertical structure, which permeates the solar atmosphere and can channel plasma towards the upper

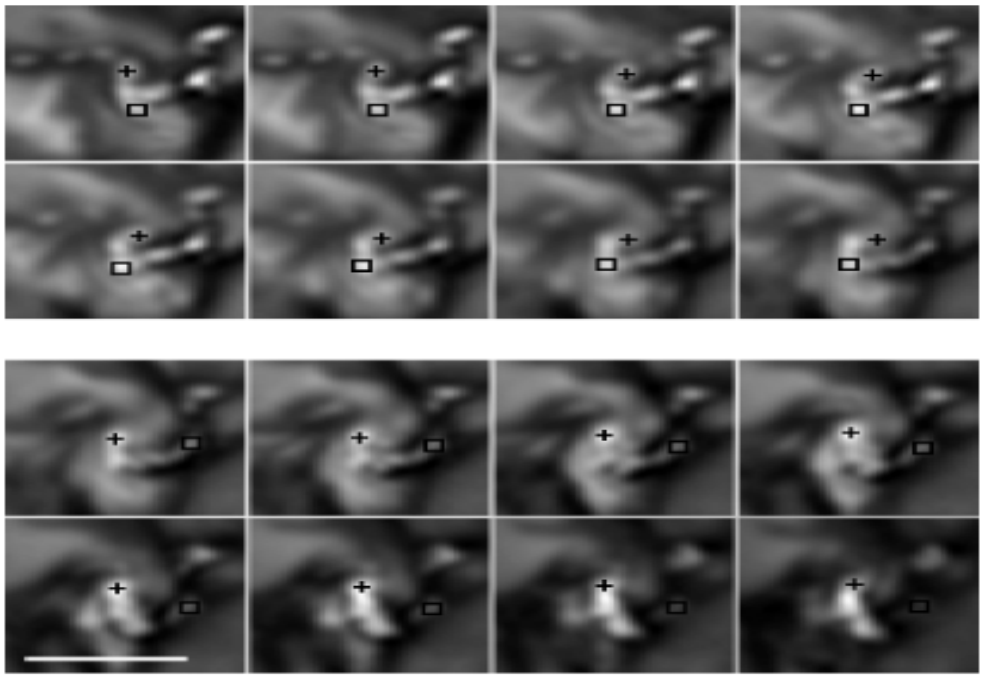

Figure 1.1: Sequence of snapshots separated by 15 s, from approximately 1 Mm x 1 Mm parcel of the photosphere. Box and cross signs are used to better show regions which are magnetic bright points (BP). One can see that these BPs rotate with respect to each other. Figure obtained from Bonet et al. (2008).

layers through spiral trajectories. The gas is accelerated upwards and outwards by the centrifugal force, while torsional Alfvén waves transport considerable amounts of Poynting flux to the lower corona. This finding established vortices and swirls as potential contributors to coronal heating.

1.2 Vortices in numerical simulations

With the development of better hardware and codes to simulate the solar atmosphere, the study of vortex flows in numerical simulations gained popularity. Many numerical simulations have been performed, all with different resolutions and different magnetic configurations (Table 1.2). Vortex flows are a common feature in those simulations, although their properties generally depend on the specifics of the numerical simulations. Table 1.2 indicates some of those characteristics and the numerical codes employed by different studies. Stein & Nordlund (1998) used hydrodynamic simulations to show that vorticity generation in the upper convection zone is mainly due to baroclinicity. The misalignment of the pressure and density gradients due to convection is the main mechanism to produce vortex flows. Shelyag et al. (2011) showed that the generation of vorticity at the visible solar surface of non-magnetic models comes from the hydrodynamic baroclinic term.

Vortex flows can be produced in the convection region and photosphere from pure hydrodynamic simulations, but magnetic fields are required for the propagation of vorticity to the upper solar atmospheric layers in the form of torsional Alfvén waves. Shelyag et al. (2011) showed that vorticity generation in magnetic field concentrations is physically different from hydrodynamic simulations. In the magnetic case, magnetic tension dominates over baroclinicity in the generation of vorticity. Moll et al. (2012) compared photospheric vortices of magnetic and non-magnetic simulations and discussed the

Reference	MHD code	Initial magnetic field $\|B\|_0$	Height of lower boundary	Height of upper boundary
Hydrodynamic simulations (no or weak magnetic field)				
Muthsam et al. (2010)	ANTARES	-	-450 km	2313 km
Steiner et al. (2010)	CO^{5}BOLD	-	-1400 km	1400 km
Moll et al. (2011)	MURaM	-	-890 km	510 km
Kitiashvili et al. (2011)	SolarBox	-	-5000 km	500 km
Freytag et al. (2012)	CO^{5}BOLD	-	-2400 km	2000 km
Moll et al. (2012)	MURaM	-	-900 km	800 km
Shelyag et al. (2011b)	MURaM	-	-800 km	600 km
Steiner and Rezaei (2012)	CO^{5}BOLD	-	-1400 km	1400 km
Kitiashvili et al. (2013)	SolarBox	-	-5200 km	1000 km
Amari et al. (2015)	METEOSOL	-	-1500 km	15000 km
Calvo et al. (2016)	CO^{5}BOLD	-	-1400 km	1400 km
Magnetohydrodynamic simulations				
Vögler (2004)	MURaM	200 G	-800 km	600 km
Carlsson et al. (2010)	Bifrost	40 G	-1400 km	14100 km
Shelyag et al. (2011b, 2013)	MURaM	200 G	-800 km	600 km
Steiner and Rezaei (2012)	CO^{5}BOLD	50 G	-1400 km	1400 km
Moll et al. (2012)	MURaM	200 G	-900 km	800 km
Wedemeyer-Böhm et al. (2012)	CO^{5}BOLD	50 G	-2400 km	2000 km
Kitiashvili et al. (2013)	SolarBox	10 G	-5200 km	1000 km
Kato and Wedemeyer (2017)	CO^{5}BOLD	50 G	-2400 km	2000 km
Khomenko et al. (2018, 2021)	MANCHA3D	dynamo	-950 km	1400 km
	MANCHA3D	10 G	-950 km	1400 km
Yadav et al. (2020, 2021)	MURaM	200 G	-1500 km	2500 km
Silva et al. (2020, 2021)	MURaM	200 G	-1000 km	600 km
Rajaguru et al. (2020)	CO^{5}BOLD	50 G	-1400 km	1400 km
Battaglia et al. (2021)	CO^{5}BOLD	50 G	-1300 km	1500 km

Figure 1.2: Recompilation of hydrodynamic and magnetohydrodynamic convective simulations that have been employed to analyse the vortex motions in the simulated solar atmosphere. Figure from Tziotziou et al. (2023).

associated local heating. They found the vortex flow to be quite similar in the deep and the near-surface layers, however, in the upper photospheric layers, they were drastically different.

The method used for identifying vortical motions in numerical simulations greatly affects the study of the nature of these flows. Initial studies relied on vorticity, but most recent studies use a better and more accurate method, called "swirling strength", to identify vortex flows in numerical simulations.

1.3 Objectives and methodology

In this study, we will focus on the analysis of vortex flows in time series produced by the MANCHA code (Khomenko & Collados, 2012; Khomenko et al., 2018), which solves the MHD equations with partial ionization effects. The swirling strength and enhanced swirling strength criteria will be used for vortex identification. After identifying the vortex flows in all the time series, we will perform statistical analyses on different properties, such as the distribution of vortex volumes, the nature of these flows, variations in plasma properties (kinetic energy density, temperature, etc.) in vortex regions compared to average plasma properties. We will study the vertical component of the Poynting vector to determine if vortex regions could serve as channels for electromagnetic energy propagation in the solar atmosphere. Finally, we will evaluate the correlation between the temperature and the swirling strength, to see if these flows can be related directly to the heating of the solar atmosphere.

The organization of the manuscript is as follows. In Chapter 2 we present the numerical code used for the computation and the details of the numerical simulations. Chapter 3 focuses on the mathematical description of the aforementioned vortex identification methods. In Chapter 4, we show the results obtained from the statistical analyses of the vortices. Finally, in Chapter 5 we summarize the conclusions derived from the results and discuss possible future lines of work derived from this study.

Chapter 2

Data and simulation

The MANCHA3D code, described in Khomenko & Collados (2012), solves the non-ideal, non-linear equations of single-fluid magnetohydrodynamics (MHD), with magnetohydrostatic (MHS) equilibrium condition explicitly removed from the equations. The code incorporates ambipolar diffusion, the Hall effect, and the battery effect, which are important effects arising from the presence of neutral atoms in the solar plasma. Assuming strong collisional coupling, these effects result in additional terms in the generalized induction equation and impact the energy conservation equation, as described in Khomenko et al. (2014) and Ballester et al. (2018). González-Morales et al. (2018) detail the numerical treatment of these terms. The single-fluid approximation is well justified in the photosphere and low chromosphere, regions of most importance in this study.
In the present study, we analyze two temporal series. The duration of each simulation is 20 minutes of solar time, with a temporal cadence of 10 seconds, for a total of 120 snapshots. The main difference between these two temporal series is the initial magnetic field configuration, one presenting a chaotic magnetic field configuration produced from local dynamo effects (called $Dynamo$ from now on), and the other one initiated from a vertical magnetic field with a mean flux of 50 G, and having more structured and regular field (called $50G$ from now on).

All snapshots present the same spatial resolution, featuring a mesh of $288 \times 288 \times 168$ spatial points. The x-y planes consist of 288×288 points with a grid spacing of $dx = dy = 20$ km, and the vertical z-direction presents 168 spatial points with a resolution of $dz = 14$ km. This corresponds to approximately $5.7 \times 5.7 \times 2.3$ Mm section of the Sun, spanning from the convection region ($z \sim -952$ km) to the lower chromosphere ($z \sim 900$ km).
The simulation is periodic in the horizontal x and y directions, and has an open bottom boundary with controlled mass and energy flux, and a top boundary closed for mass flows. The first and last five points in the vertical direction correspond to the boundary condition, and therefore are not physical and are removed from the analysis.

From these snapshots, we obtain a complete description of the plasma and the underlying magnetic field, enabling us to extract information regarding temperature (T), pressure (p), density (ρ), and electron density (ρ_{e^-}), as well as the 3D velocity field $\boldsymbol{v}$ (v_x, v_y, v_z), and the 3D magnetic field $\boldsymbol{B}$ (B_x, B_y, B_z), all expressed in SI units.

In figures 2.1 and 2.2 we can see the vertical velocity and magnetic field maps at the photosphere. We can see the typical pattern from convection cells, indicating us that convection indeed takes place in both simulations, and we are simulating the plage region. Also we should remark, that there are no important magnetic structures like sunspots, which can also be simulated with the MACHA code.

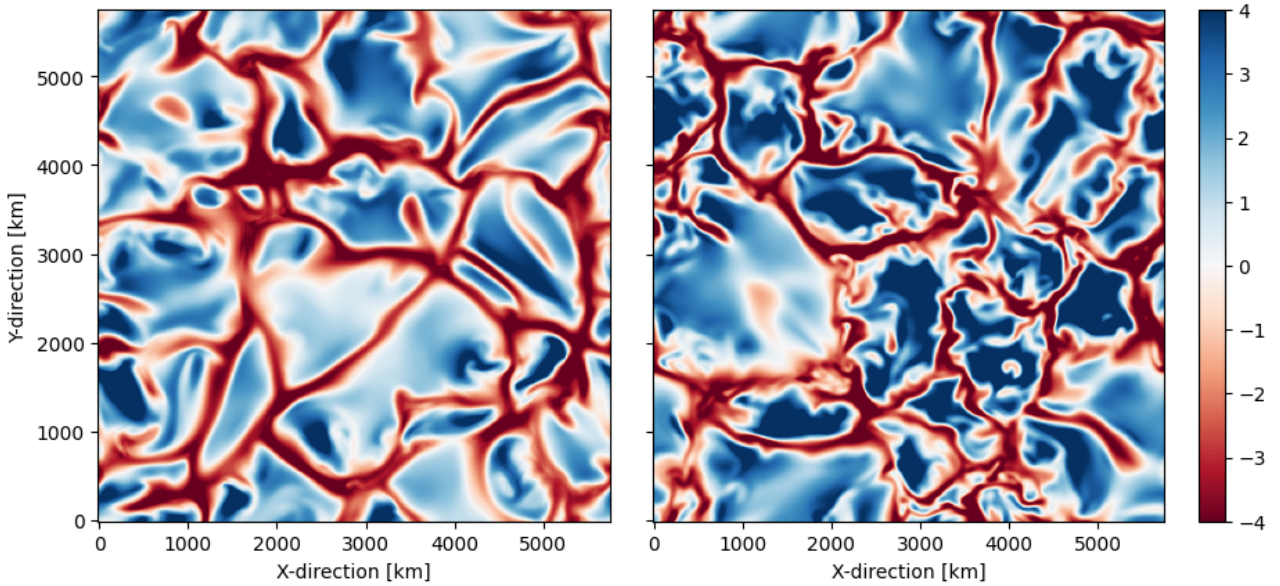

Figure 2.1: Vertical velocity (v_z) maps at the photosphere, saturated at 4 km/s for downwards and upwards flows. Left: $Dynamo$. Right: $50G$.

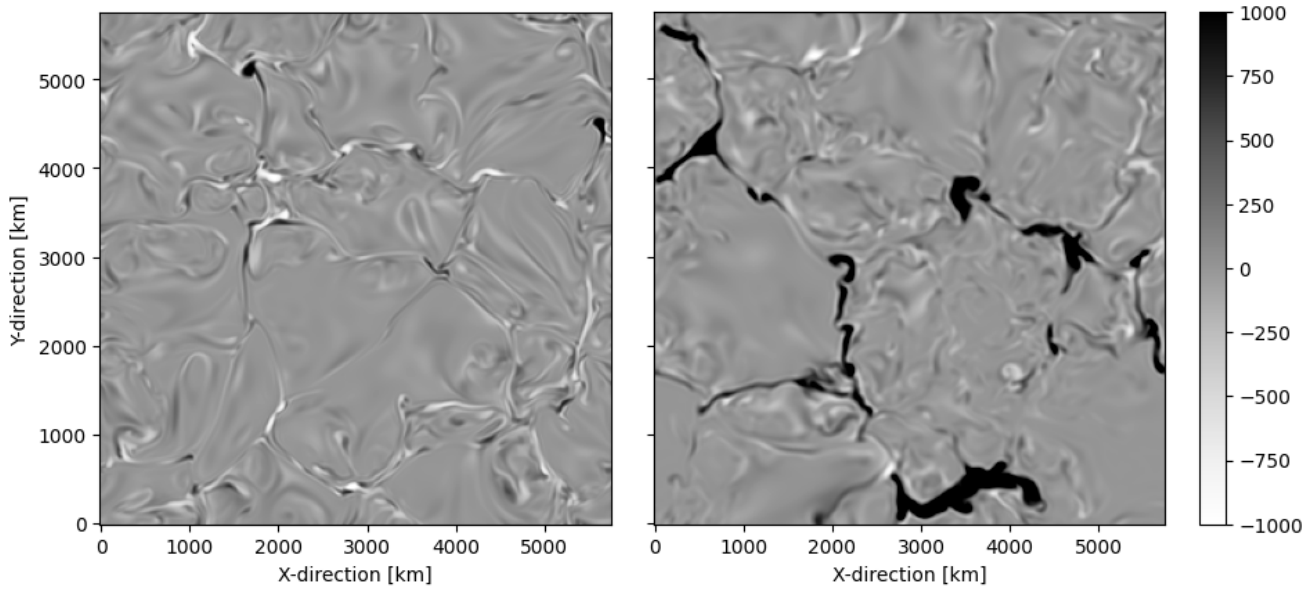

Figure 2.2: Vertical magnetic field (B_z) maps at the photosphere, saturated at 1000 G for both directions. Left: $Dynamo$. Right: $50G$.

Chapter 3

Vortex identification criterion

In this Chapter, we are going to show the mathematical description of how the vorticity is generated in the simulations. After it, the swirling strength and enhanced swirling strength criterion, used for the identification of vortices, will be presented, in addition to some images of the identifications.

Initial studies relied on vorticity ($\vec{\omega} = \boldsymbol{\nabla} \times \vec{v}$) to indentify vortex flows. However, this parameter is not ideal as it cannot distinguish between vortex and shear flows, leading to false interpretations. Zhou et al. (1999) proposed a new method called the swirling strength, based on the analysis of the eigenvalues and eigenvectors of the velocity gradient tensor. This method has been shown to accurately identify vortex flows and has been used in many studies of solar vortical motions (Moll et al., 2011; Kato & Wedemeyer, 2017; Battaglia, 2021).

Chakraborty et al. (2005) developed the enhanced swirling strength method, which is based on the swirling strength. This new method relies on three requirements for a vortex flow to be identified: (1) Galilean invariance of the criterion, (2) the flow must be swirling in a reference frame moving with the vortex, and (3) the trajectories within the vortex flow must be compact. The first two requirements are fulfilled by the swirling strength criterion, but the third requirement is not. To address this, the authors defined the inverse spiraling compactness ratio from the same eigenanalysis, adding a new restriction for vortex flow identification.

3.1 Generation of vorticity

To investigate vortices in the solar atmosphere, it is crucial to derive an evolution equation for vorticity that allows for the examination of different source terms that generate vorticity. To obtain the vorticity equation, we must rewrite the standard MHD momentum equation in the following form:

$$\frac{\mathrm{d}\boldsymbol{v}}{\mathrm{d}t} = -\frac{1}{\rho}\nabla\left(p_{\mathrm{g}} + p_{\mathrm{m}}\right) + \frac{1}{\rho}(\boldsymbol{B}\cdot\nabla)\boldsymbol{B} \tag{3.1}$$

Where, $\boldsymbol{B}$ is the magnetic field, $\boldsymbol{v}$ is the plasma flow velocity, ρ is the plasma mass density, p_g and $p_m = \frac{B^2}{2\mu_0}$ are the thermal gas and magnetic pressure, and $\frac{d}{dt} = \frac{\partial}{\partial t} + (\boldsymbol{v}\cdot\boldsymbol{\nabla})$ is the total material derivative.

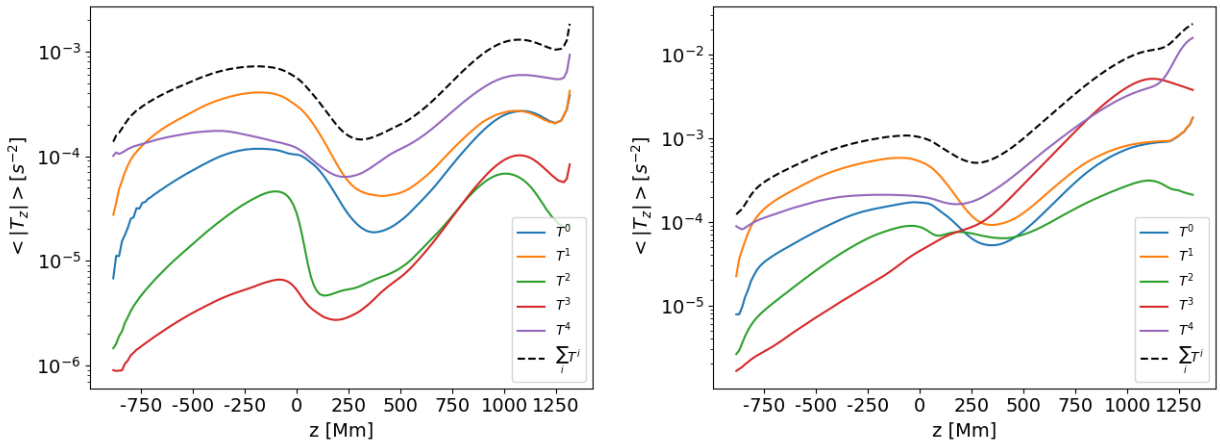

Figure 3.1: Horizontally and temporally averaged terms from equation (3.3) (T^i) as a function of height (z). Left: $Dynamo$ time series. Right: $50G$ time series.

Expanding the material derivative and using the following vector identity $(\boldsymbol{u}\cdot\nabla)\boldsymbol{u} = \frac{1}{2}\nabla\boldsymbol{u}^2 - \boldsymbol{u}\times(\nabla\times\boldsymbol{u})$ we get:

$$\frac{\partial \boldsymbol{v}}{\partial t} + \frac{1}{2}\nabla\boldsymbol{v}^2 - \boldsymbol{v}\times\boldsymbol{\omega} = -\frac{1}{\rho}\nabla\left(p_{\mathrm{g}} + p_{\mathrm{m}}\right) + \frac{1}{\rho}(\boldsymbol{B}\cdot\nabla)\boldsymbol{B} \tag{3.2}$$

Here $\boldsymbol{\omega} = \nabla\times\boldsymbol{v}$ is the vorticity vector. Taking the curl of Eq. (3.2) and calling the vector identity $\Phi\times\nabla\Phi = 0$, where Φ is a scalar quantity, one arrives at the evolution equation of vorticity:

$$\frac{\partial\boldsymbol{\omega}}{\partial t} + (\boldsymbol{v}\cdot\nabla)\boldsymbol{\omega} = \underbrace{-\boldsymbol{\omega}(\nabla\cdot\boldsymbol{v})}_{T^0}\underbrace{+(\boldsymbol{\omega}\cdot\nabla)\boldsymbol{v}}_{T^1}\underbrace{-\nabla\frac{1}{\rho}\times\nabla p_{\mathrm{g}}}_{T^2}\underbrace{-\nabla\frac{1}{\rho}\times[\nabla p_{\mathrm{m}} - (\boldsymbol{B}\cdot\nabla)\boldsymbol{B}]}_{T^3}\underbrace{+\frac{1}{\rho}\nabla\times[(\boldsymbol{B}\cdot\nabla)\boldsymbol{B}]}_{T^4} \tag{3.3}$$

The different T^i are defined in the same way as in Canivete Cuissa & Steiner (2020) (Eq. (3)). As the authors explain in their work, T^0 and T^1 terms directly depend on the vorticity and are called vortex stretching and vortex tilting terms, respectively. T^2 is the hydrodynamic baroclinic term, which is responsible for the generation of vorticity when the gradients of density and pressure are not parallel. Finally, we encounter two terms that are related to the magnetic field T^3 and T^4. The first shall be called magnetic baroclinic term, since it is the magnetic equivalent to T^2, and the last one is related to magnetic tension.

As discussed by several authors (e.g., Canivete Cuissa & Steiner, 2020; Shelyag et al., 2011), these terms depend on height (z-coordinate), leading to differences in the main mechanism responsible for the generation of vorticity in the different layers of the solar atmosphere.

Figure 3.1 shows the height dependence of the different T^i terms from the evolution equation of vorticity for both time series. We computed the T^i terms for all spatial locations in all the snapshots for both time series. Then, we obtained the horizontal average to get a general behaviour of the whole simulated box, and finally, we did a temporal average to remove the 5-minute global oscillations from the simulated box.

As we can see for the $Dynamo$ time series, in the solar interior the vorticity is generated mostly by hydrodynamic

effects, dominated by T^1 (orange color), followed closely by the magnetic tension term, T^4 (violet color). As we go to the solar surface and the solar atmosphere, these two terms exchange their importance. This is indicating us that the magnetic field structure (specifically the magnetic tension) in the solar atmosphere plays a more important role in the generation of vortices. The T^0 is the third most important term in this temporal series, for all the heights, being as important as T^1 at the top of the simulated box.

For the $50G$ time series, in the solar interior, the generation of vorticity presents the same structure as the $Dynamo$ time series. The dominance of T^1 with T^4 being the second most important. In contrast, differences are found in the solar atmosphere, where both magnetic terms T^3 and T^4 dominate completely the generation of vorticity. This is expected since this temporal series has a mostly vertical initial magnetic field configuration imposed, so the magnetic structures are much stronger and therefore magnetic effects play an important role. The hydrodynamic effects are at least one order of magnitude less important in the solar atmosphere, so they can be neglected (at least in the first order) for the generation of vortices.

Finally, we have compared the total of the vorticity terms for both time series. The $50G$ time series presents a steeper slope, getting the black-dashed line ($\sum_i T^i$) to values around 10^{-2} [s^{-2}] at the top of the box, whereas in $Dynamo$ the maximum value is an order of magnitude lower 10^{-3} [s^{-2}]. In the solar interior, both time series exhibit almost the same order of magnitude for the different terms, but in the solar atmosphere, the $50G$ time series has much stronger vorticity values .

3.2 Swirling strength

Zhou et al. (1999) proposed this method of identification and it has been widely used in solar physics (Moll et al., 2011; Kato & Wedemeyer, 2017; Battaglia, 2021). This method presents an important advantage concerning the simple vorticity analysis: swirling strength is not affected by the presence of shear flows.

This method relies on the eigenanalysis of the velocity gradient tensor $\mathcal{U}_{ij} \equiv \partial_j v_i$,

$$\mathcal{U} = \begin{pmatrix} \partial_x v_x & \partial_y v_x & \partial_z v_x \\ \partial_x v_y & \partial_y v_y & \partial_z v_y \\ \partial_x v_z & \partial_y v_z & \partial_z v_z \end{pmatrix} \tag{3.4}$$

which physically encodes local variations of the velocity field.

Diagonalizing $\mathcal{U}$ gives information about the flow of the plasma. In a vortex region, the velocity gradient tensor presents a complex conjugated pair of eigenvalues and simple real eigenvalue (Chong et al., 1990), so we can do a change of basis and rewrite the velocity gradient tensor as:

$$\mathcal{U} = \underbrace{(\boldsymbol{u}_\mathrm{r}, \boldsymbol{u}_+, \boldsymbol{u}_-)}_{\mathcal{P}} \begin{pmatrix} \lambda_\mathrm{r} & 0 & 0 \\ 0 & \lambda_+ & 0 \\ 0 & 0 & \lambda_- \end{pmatrix} \underbrace{(\boldsymbol{u}_\mathrm{r}, \boldsymbol{u}_+, \boldsymbol{u}_-)^{-1}}_{\mathcal{P}^{-1}} \tag{3.5}$$

where λ_r, λ_+ and λ_- are the eigenvalues of $\mathcal{U}$, while $\boldsymbol{u}_r$, $\boldsymbol{u}_+$ and $\boldsymbol{u}_-$ are the corresponding eigenvectors that form the change-of-basis matrix $\mathcal{P}$ and its inverse $\mathcal{P}^{-1}$.

The pair of complex conjugated eigenvalues can be rewritten in a simple real-imaginary part notation $\lambda_{\pm} = \lambda_{cr} \pm i\lambda_{ci}$. Similarly, we can rewrite the complex eigenvectors as $\boldsymbol{u}_{\pm} = \boldsymbol{u}_{cr} \pm \boldsymbol{u}_{ci}$. This is done to extract physical information about the local motions.
The imaginary part of the complex eigenvalues λ_{ci} defines the strength of the local swirling motions, and it's related to the period T of a particle in a purely rotational vortex by $T = 2\pi/\lambda_{ci}$ (Zhou et al., 1999).

Additionally, we can obtain information about the vortex axis (direction around which the flow is rotating or spiraling) since $\boldsymbol{u}_r$ defines it. We can define the swirling strength vector as $\boldsymbol{\lambda} = \lambda \boldsymbol{u}_r$, where $\lambda = \lambda_{ci}$, which provides the strength, the direction, and the orientation of the vortex, but one must ensure the correct orientation of the vortex axis (according to the right-hand rule), choosing $\boldsymbol{u}_r$ which satisfies Im[det(P)] > 0, where P is the change-of-basis matrix defined before (Canivete Cuissa & Steiner, 2020).
A more detailed explanation of the meaning of the different eigenvalues can be seen in Canivete Cuissa & Steiner (2020) appendix A. In summary, they can be interpreted in the following way:

- λ_r : a measure of how the flow is stretched or compressed along the direction given by $\boldsymbol{u}_r$.
- λ_{cr} : a measure how stretched is the flow in the rotation plane (defined by $\boldsymbol{u}_{cr}$ and $\boldsymbol{u}_{ci}$).
- λ_{ci} : a measure of the strength of the swirling motion and the $\boldsymbol{u}_r$ vortex axis.

In this work, we will use the same definition as Canivete Cuissa & Steiner (2020). In their work, they define the swirling strength as $\lambda = 2\lambda_{ci}$ to ensure that, for a rigid-body rotation, both swirling strength and vorticity return the same value $\lambda = \omega = 4\pi/T$.

Finally, a threshold value (ϵ) must be imposed on the criteria to only identify regions with a clear swirling motion. In our definition we get:

$$\lambda = 2\lambda_{ci} \geq \epsilon > 0 \tag{3.6}$$

The threshold value used for our study will be defined later in this chapter.

3.3 Enhanced swirling strength

This method was proposed by Chakraborty et al. (2005). As the name suggests it enhances the swirling strength criteria by defining the inverse spiraling compactness ratio ($\xi = \frac{\lambda_{cr}}{\lambda_{ci}}$), where λ_{cr} and λ_{ci} are the same real and imaginary parts of the eigenanalysis from the last section.

The inverse spiraling compactness is a measure of the radial distance traveled by a test particle in the flow during one orbital period. So we can identify three cases:

- $\xi = 0$: the flow is perfectly circular
- $\xi > 0$: the flow is spiraling outwards
- $\xi < 0$: the flow is spiraling inwards

It is easy to see that if ξ presents large (either positive or negative) values it is an indication of very low spiraling compactness. Therefore regions identified with the swirling strength criteria with $|\xi|$ too big should be discarded, since in these cases the orbital component of the velocity field is negligible compared to the radial one, so the rotational motion is barely noticeable.
In practice, we define a new threshold parameter κ that can be adjusted according to the compactness required. We only identify as vortices the regions where $|\xi| > \kappa$, in addition to the criterion from Eq. 3.6.

3.4 Application of the methods to the data

Since we are working with data from simulations, we have complete information on the velocity fields in each point of the 3D space. This allows us to compute the velocity gradient tensor numerically in the whole simulated domain, giving us a 3x3 matrix in each grid point. Then, we perform a diagonalization of the velocity gradient tensors obtained, to perform the eigenanalysis explained before so we can compute a map of the swirling strength.
Once these maps are obtained we will use two simple thresholds:

- Enhanced swirling strength criteria.
- We compute a normalization to the swirling strength maps: at each height, we compute the 90th percentile of the non-zero swirling strength points and divide the whole 2D (x-y) sheets for the corresponding value and finally apply a simple threshold value (Eq. (3.6)).

This normalization is performed to maintain all heights at a constant threshold.

Once these swirling strength maps are computed, we make use of a connected component labeling algorithm to label each vortex region. This allows us to compute the 3D position of the vortex points, centroids and their volumes. We impose that all the vortex regions identified with volumes smaller than 27 pixels are deprecated since we assume these regions are too small and do not represent physical vortex flows.

Figures 3.2 and 3.3 illustrates the comparison between the non-filtered and filtered (according to the above criteria) swirling strength maps for both $50G$ and $Dynamo$ time series. The underlying vertical magnetic field is plotted in each case.

As we can see, the original swirling strength map (left) shows a lot of regions where this parameter is greater than zero. After all the different thresholds and filters explained before are applied we get the map from the right, where all black regions are identified as vortices. Most of the vortices lie on the vertical flux tube regions. This is expected since the underlying magnetic field structure (specifically T^3 and T^4 from eq. (3.3)) is the main generator of vorticity in the solar chromosphere, as discussed in the first section of this chapter.

In Figures 3.4 3.5 we can see the identified vortices over the underlying vertical velocity maps in the same time step as Figs. 3.2 and 3.3, both for a photospheric layer and the same chromospheric layer.

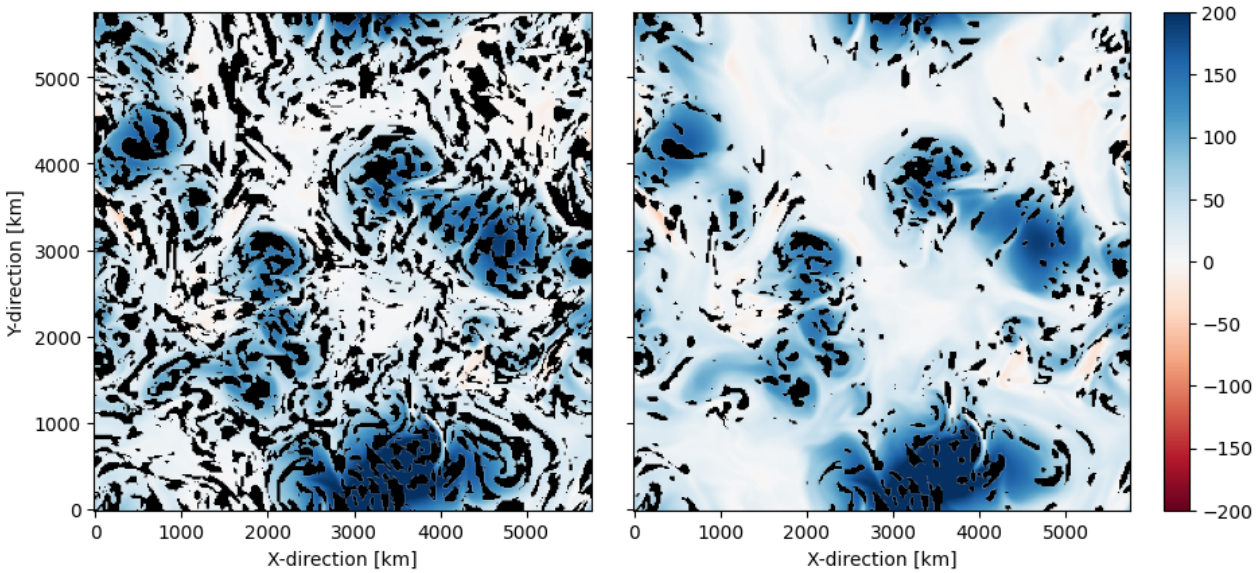

Figure 3.2: 2D maps from $50G$ of B_z [G] at a given height (z=728 km) and randomly chosen time step with overlapping non-zero swirling strength regions (left panel) and vortices identified (right panel) in black.

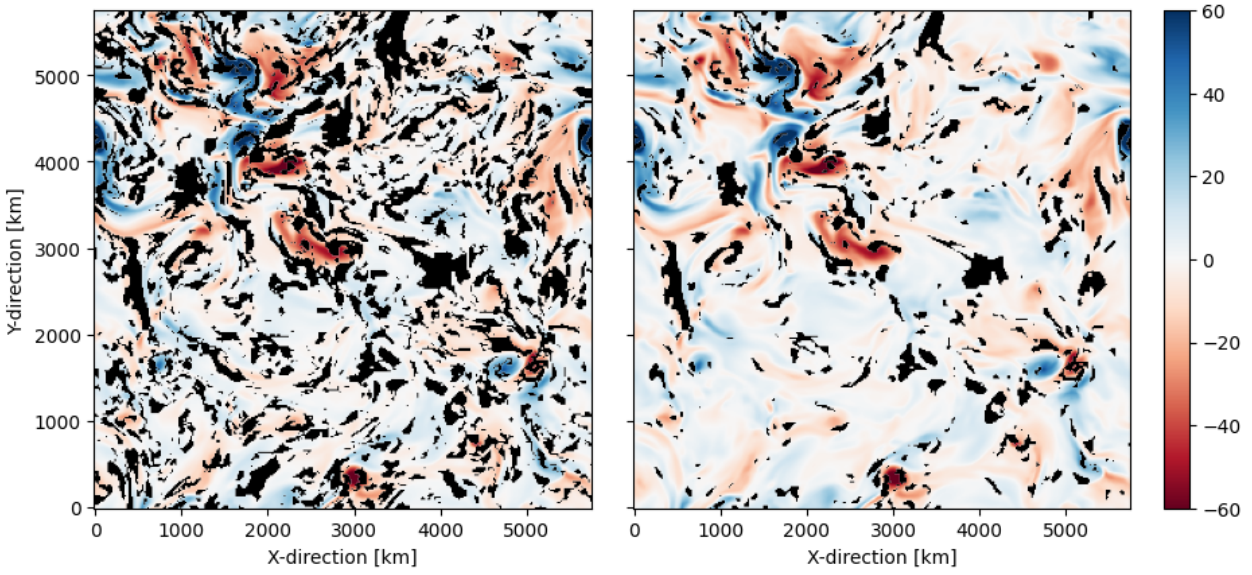

Figure 3.3: Same figure as 3.2 for $Dynamo$.

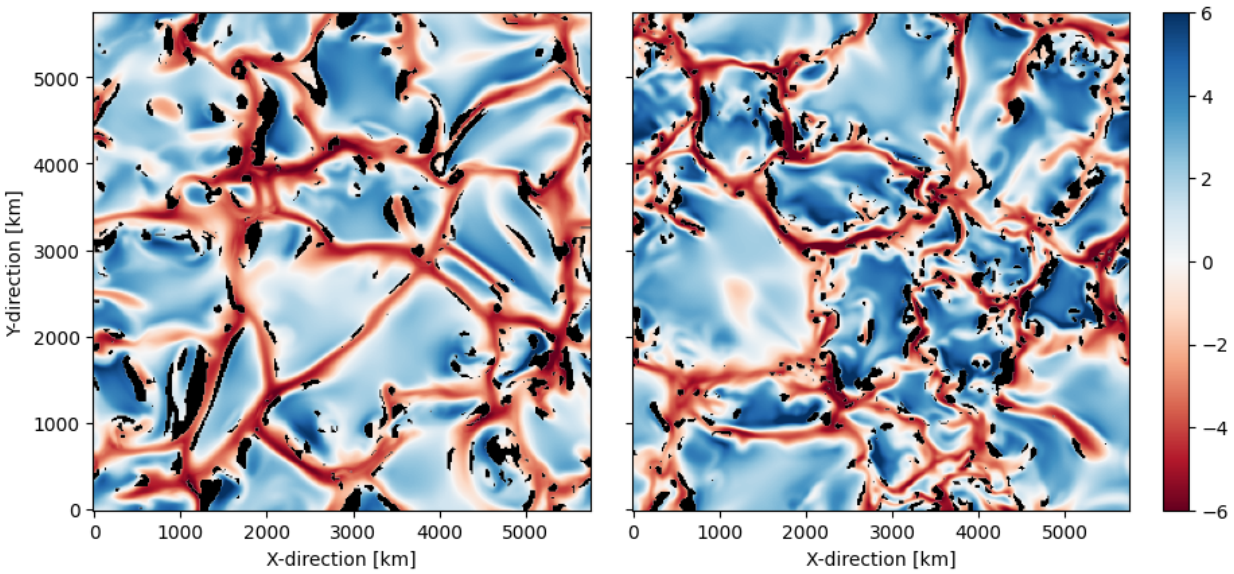

Figure 3.4: Vertical velocity maps (km/s) at the photosphere (z=0 km) with overlapping vortices identified in black. Left: $Dynamo$. Right: $50G$.

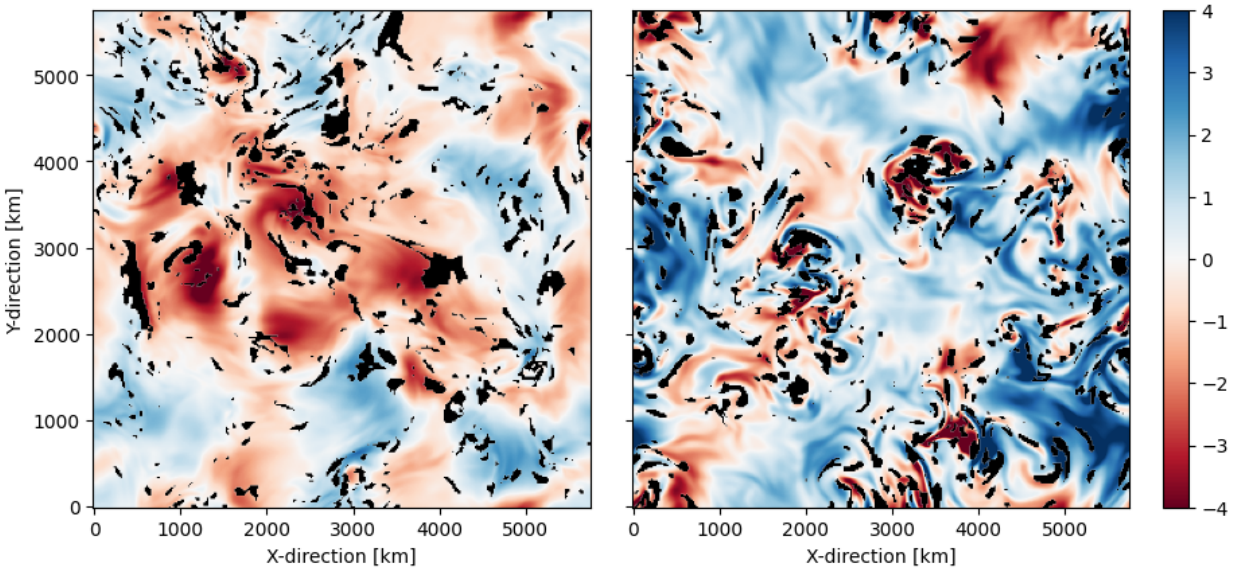

Figure 3.5: Vertical velocity maps (km/s) at the photosphere (z=768 km) with overlapping vortices identified in black. Left: $Dynamo$. Right: $50G$.

Chapter 4

Statistical analysis of vortices

In this chapter, we will present the different analyses performed in this work. First of all, we will show the statistics of the physical properties of the identified vortices, such as their volume or their area in horizontal planes. After this, we will present the differences in the plasma properties between vortices and non-vortices regions.

4.1 Morphology and structure

As indicated in the previous chapter, we only considered connected regions of at least 27 pixels as vortices. This threshold on the size is based on the assumption that the smallest coherent structure that could form a vortex is a $3 \times 3 \times 3$ pixels cube, that would have a physical extension of around 60 km in each direction. Other authors, like Yadav et al. (2021), propose that only structures of at least 200 connected pixels should be considered (with pixel size of 10 km in all directions), to avoid transient structures. Despite the differences in the identification criterion and in the configuration of the numerical simulations (Yadav et al. (2021) employed a stronger initial magnetic field and finer spatial resolution), the physical extension of the structures reported in previous studies is comparable to our results.

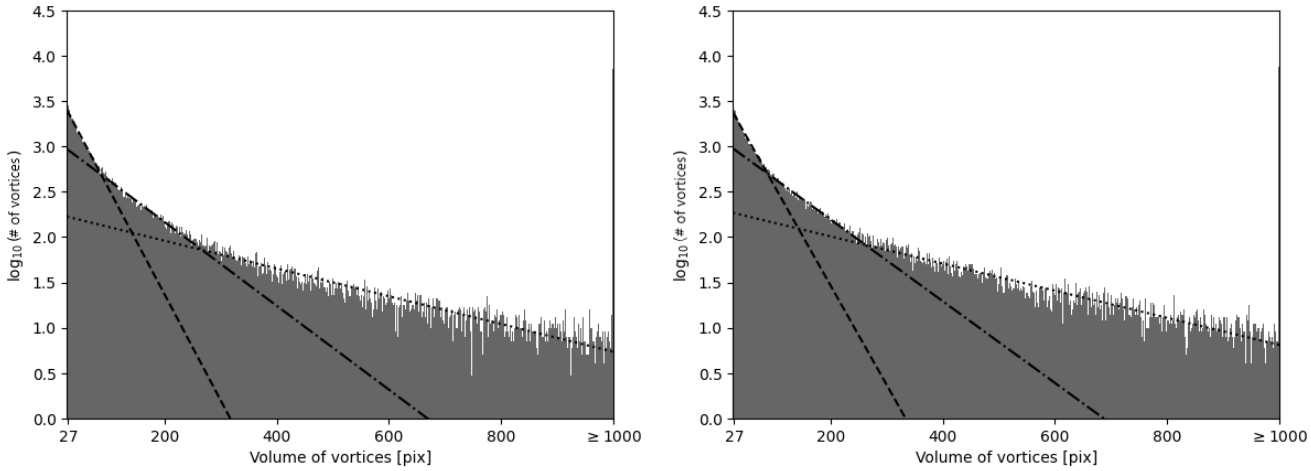

Figure 4.1: Histograms of the volume (pix) of the vortices identified in the full-time series. Left: $Dynamo$ time series. Right: $50G$ time series. Dashed line: Fit for small volume region. Dotted-dashed line: Fit for medium volume region. Double-dotted-dashed line: Fit for big volume region.

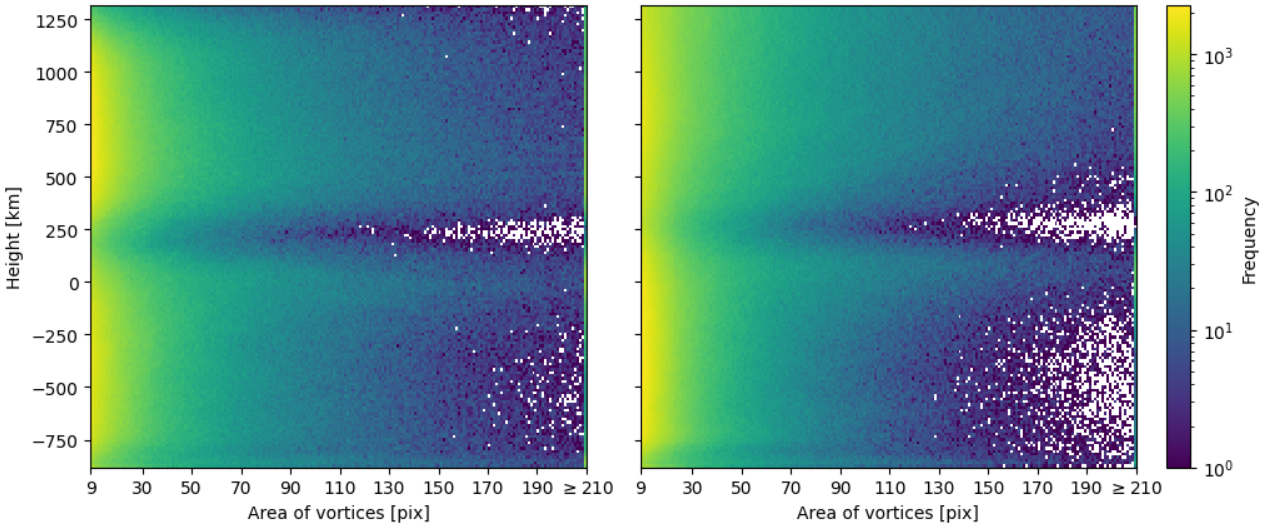

Figure 4.2: Height-area 2D histograms for identified vortices in $Dynamo$ (left) and $50G$ (right) whole time series. White pixels represent 0 vortices were identified in the corresponding bin.

As we can see in Fig. 4.1, both time series present a similar histogram for the volume (in pixels) of the identified vortices. Both figures have a logarithmic y-axis, and they do not follow a linear trend. We have characterized the distribution of the volumes by identifying three different regions.

The small-scale region includes volumes from 27 up to 85 pixels, approximately. The medium-scale vortices span from 85 to 225 pixels approximately. Finally, the big-scale vortices are those bigger than 225 pixels in volume. Each region has been fitted to a 1st-degree polynomial in the log-scale (so an exponential fit in the linear scale), of the form $log(\text{Frequency}) = m \cdot \text{Volume [pix]} + n$. The following table illustrates the results from the fits:

	Small volume [27, ≈85) [pix]	Medium volume ≈(85, 225) [pix]	Big volume ≳225 [pix]
	m / n	m / n	m / n
Dynamo	-1.17e-2 / 3.70	-4.62e-3 / 3.09	-1.53e-3 / 2.26
50G	-1.10e-2 / 3.65	-4.50e-3 / 3.09	-1.50e-3 / 2.31

Table 4.1: Linear fits of pixel volume histograms for the three different scales identified.

Both time series present very small differences in the fits performed for each scale. This indicates that the initial magnetic configuration does not significantly affect the volume distribution of the identified vortices.

As other authors have pointed out (Yadav et al., 2021; Shelyag et al., 2011), these properties are highly dependent on the identification criteria used and the spatial resolution of the simulation.

Figure 4.2 shows 2D area-height histograms for both time series. The figure illustrates the frequency of a certain vortex area (in horizontal 2D planes) as a function of the height. All heights are dominated by small area vortices. This is expected since regions with vorticity at small scales are easier to form and more common than big-scale regions. For

any given area, we see that a minimum appears at the photosphere. This minimum is caused by the different mechanisms for the generation of vorticity.
The solar interior is dominated by convective movements. Convection is the main generator of vorticity, which is amplified mainly through the $T^1 = (\boldsymbol{\omega} \cdot \nabla)\boldsymbol{v}$ (vortex tilting term) as shown in Figure 3.1. This term leads to the appearance of small-scale vortices mainly through hydrodynamical processes.

At the base of the photosphere $z = 0$ km, there is an increment in the frequency of detections. This is due to the conditions of the photosphere. There is no convection but overshooting is present and vorticity can still be generated by the T^1 (that presents a local maximum for both time series near $z = 0$ km). In this region, the coexistence of up-flows and down-flows forms an ideal scenario for the generation of small-scale vortices. At higher layers, convection is no longer present and the magnetic field structure gains relevance in the plasma movement. This magnetic field structure produces the generation of vorticity mainly via the T^4 term (magnetic tension term). Then, we see different results depending on the initial magnetic configuration.

In $Dynamo$, since there is no magnetic field imposed from the beginning, the hydrodynamic effects are still relevant in the chromosphere and upper layers, producing mainly small area vortices. On the other hand, in $50G$ the imposed vertical magnetic field produces the T^3 (magnetic baroclinic term) to be as important as T^4. From this result, we conclude that this magnetic vorticity generation mechanism produces bigger size vortices, along the magnetic flux tubes. Figure 4.3 illustrates the time-averaged percentage of area covered by vortices as a function of height (z). For both time

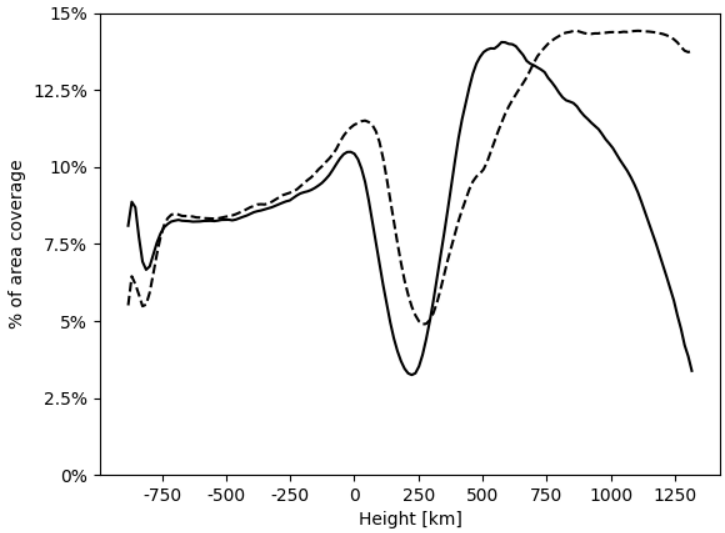

Figure 4.3: Time averaged percentage of area covered by vortices as a function of height. Solid line: $Dynamo$. Dashed line: $50G$.

series, at sub-photospheric levels the area covered by vortices is between 7.5% and 11%, increasing as we approach the photosphere. At the photosphere, we see a sudden decrease in area coverage, with a minimum of $2.5 - 5\%$ at 250 km over the surface. Finally, at the upper layers, the behavior of both simulations exhibits striking differences. In $Dynamo$, we see a maximum in area coverage (14%) at the low chromosphere (750 km). Above that layer, the area coverage dramatically decreases. In the case of the $50G$ simulation, we see a similar increment in area coverage reaching close

to the same value (14%) at the same height, but this value remains almost constant along the upper layers of the solar atmosphere.

All these results can be appreciated in a 3D visualization of the vortices detected in a snapshot from both time series (Fig. 4.4). The general 3D structure of the swirling strength illustrated in this figure is maintained through all the snapshots for both time series.

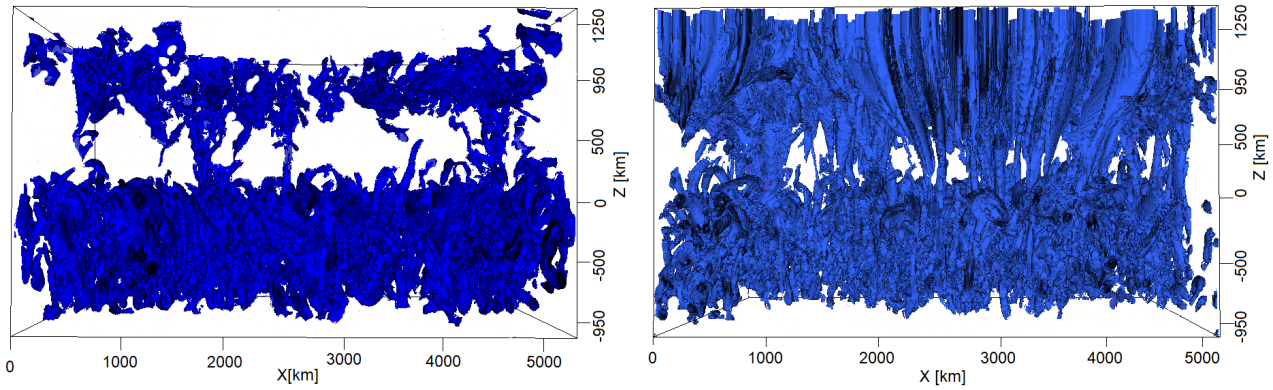

Figure 4.4: 3D visualization of the swirling strength maps from a random snapshot obtained after the application of all the filtering criteria. Left: $Dynamo$. Right: $50G$

At sub-photospheric levels, both simulations present the same 3D structure for vortices. They appear as elongated irregular tubes with the main axis pointing mostly vertically with tilting. This is expected since the vortical flows are mainly generated through hydrodynamical processes. These vortices are often called Intergranular Vortex Flows (IVF) in the literature, cause they mostly form in the vertices of intergranular lanes where there is an absence of strong magnetic field lines and the "bathtub effect" (for more information on the bathtub effect refer to Sec. 3.3 of Nordlund (1985)) dominates. This fact is better illustrated in Fig. 3.4, which shows a 2D visualization of the velocity field in a low photospheric layer at a randomly chosen time step of both simulations. We can see from visual inspection that for both time series, vortices in these layers form in the integranular lanes of convection.

Figure 4.4 shows that at photospheric levels, there is a clear gap in the presence of vortices for both time series. Some of the largest vortices are the lower ends of chromospheric vortices, that connect both regions. This connection has been proposed, by many authors, to be a good mechanism for the energy and material transport from the inner layers of the solar atmosphere to the outer layers. Wedemeyer & Steiner (2014) suggest that an IVF is an essential prerequisite for the formation of an atmospheric vortex flow (vortex flows in the solar atmosphere), where also a magnetic flux concentration that becomes spatially co-located with an IVF is needed. This can explain the absence of vortices in the photosphere. An encounter between a sub-photospheric vortex flow and a magnetic flux footpoint is required to form a vortex flow that connects the solar interior with the solar atmosphere. As seen in Fig. 4.4, $50G$ presents more of these vortices due to the initial vertical magnetic field configuration, making the aforementioned prerequisites more common.

At higher layers, there is an increase in the area coverage of detected vortices. This increase is probably related to the widening of the magnetic structures as one goes to higher layers in the solar atmosphere. The differences in the general structure of chromospheric vortices between both simulations are noteworthy. In $Dynamo$, the chromospheric vortices are almost identical in general structure to the sub-photospheric ones, short and tilted. For $50G$, we see long

and almost purely vertical tubes, that surround the magnetic flux tubes.

These differences can again be understood from Fig. 3.1. In $Dynamo$, two hydrodynamic terms, T^0 and T^1 (combined) are the most important contributors to the generation of vorticity (even though T^4 is the single most important, hydrodynamic effects dominate). In $50G$, the magnetic terms dominate, indicating that the formation of vortices depends almost only on the magnetic field structure.

4.2 Channels for energy propagation

The heating of the solar chromosphere and corona is an open problem in solar physics. Many solutions have been proposed and studied but there is no general agreement on all the mechanisms involved in this process. In this context, solar vortex flows have been proposed to be an important mechanism (Yadav et al., 2021; Wedemeyer-Böhm et al., 2012; Moll et al., 2012). Mainly, vortices have been proposed to be channels for the propagation of energy from the inner layers to the outer layers. Also, some authors claim that vortices are direct contributors to the heating, through viscous or ohmic dissipation, due to their localization in a magnetized medium and their highly dynamical behavior Wedemeyer & Steiner (2014). Recent studies (Khomenko et al., 2021) also show that vortices can be dissipative structures, through the ambipolar diffusion mechanism.

To study vortex flows as methods for propagating energy, we have computed the height dependency of the vertical component of the Poynting vector density inside/outside of vortex flows and compared them. We have also performed the same study for the kinetic energy density. Finally, we show 2D histograms of swirling strength and temperature at different heights to check for correlations between swirling motions and temperature.

4.2.1 Poynting flux

In MHD, the Poynting vector can be described as

$$\boldsymbol{S} = \frac{1}{\mu_0}\boldsymbol{B} \times (\boldsymbol{v} \times \boldsymbol{B}),$$

where μ_0 is the vacuum magnetic permeability, $\boldsymbol{B}$ is the magnetic field, and $\boldsymbol{v}$ is the velocity field.
We are mostly interested in the vertical component of this vector, to see if there is propagation of electromagnetic energy vertically. It can be written as

$$S_z = \frac{1}{\mu_0}(B_x \cdot (v_z \cdot B_x - v_x \cdot B_z) - B_y \cdot (v_y \cdot B_z - v_z \cdot B_y)).$$

Following Shelyag et al. (2012), we can split this term into "shear" and "emergent" terms:

$$S_z^{emer} = \frac{v_z}{\mu_0} \cdot (B_x^2 + B_y^2)$$
$$S_z^{shear} = -\frac{B_z}{\mu_0} \cdot (B_x \cdot v_x + B_y \cdot v_y)$$

The "shear" term corresponds to horizontal motions along vertical flux tubes. The "emergent" term corresponds to horizontal magnetic field perturbations carried by vertical plasma motions.

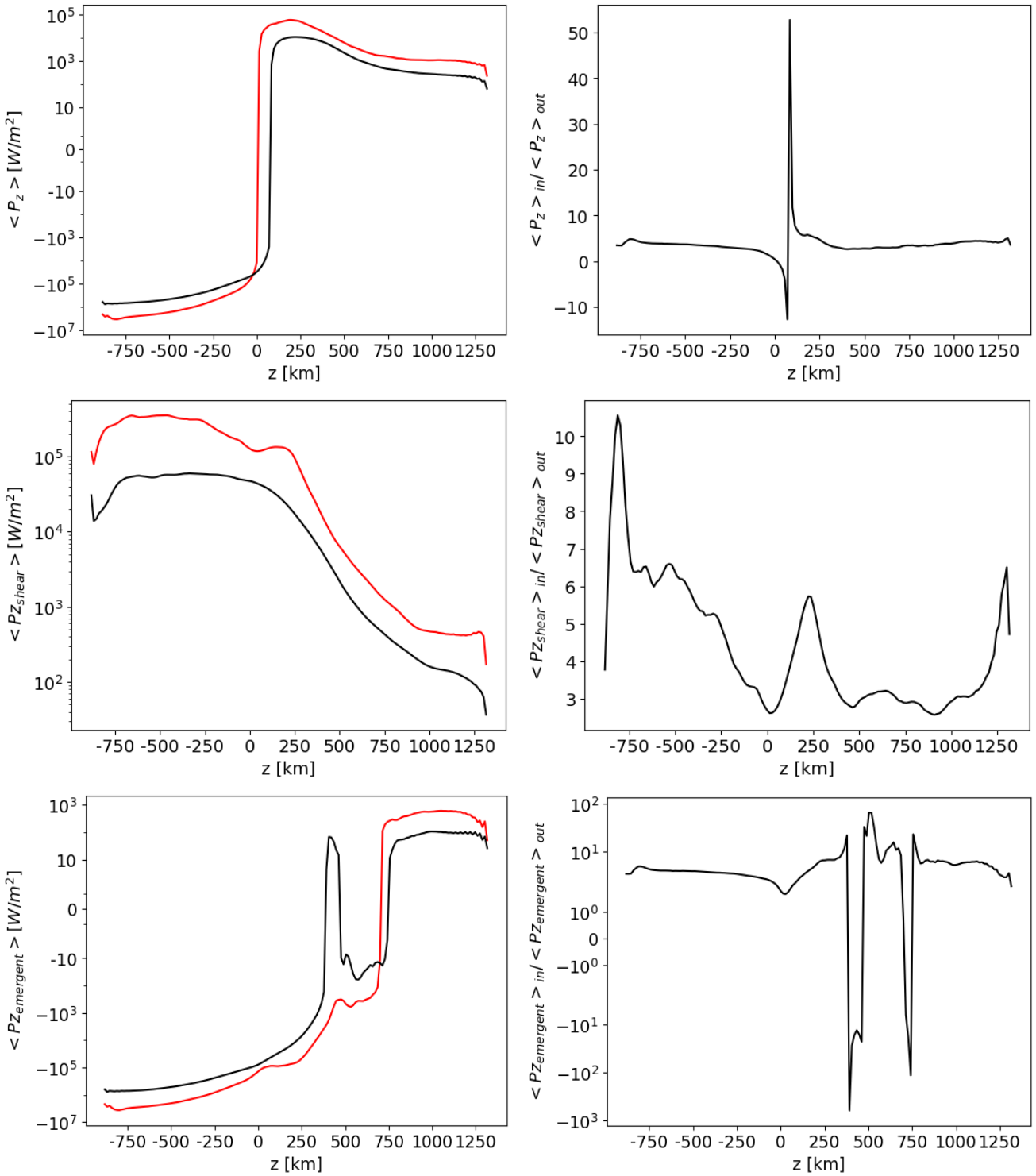

Figure 4.5: Horizontally and temporal averaged vertical Poynting flux as a function of height for $Dynamo$ simulation with "symlog" y-axis when needed. Left panels: calculation for regions identified as vortex flows (red) and non-vortex regions (black). Right panels : Ratio between "inside" of vortices (red) and "outside" of vortices (black) in absolute value. Top panels: Total vertical Poynting flux. Middle panels: "Shear" component. Bottom panels: "Emergent" component. For all the calculation we mantained the sign of the values, since it indicates if the vertical component of Poyting flux vector points upwards or downwards.

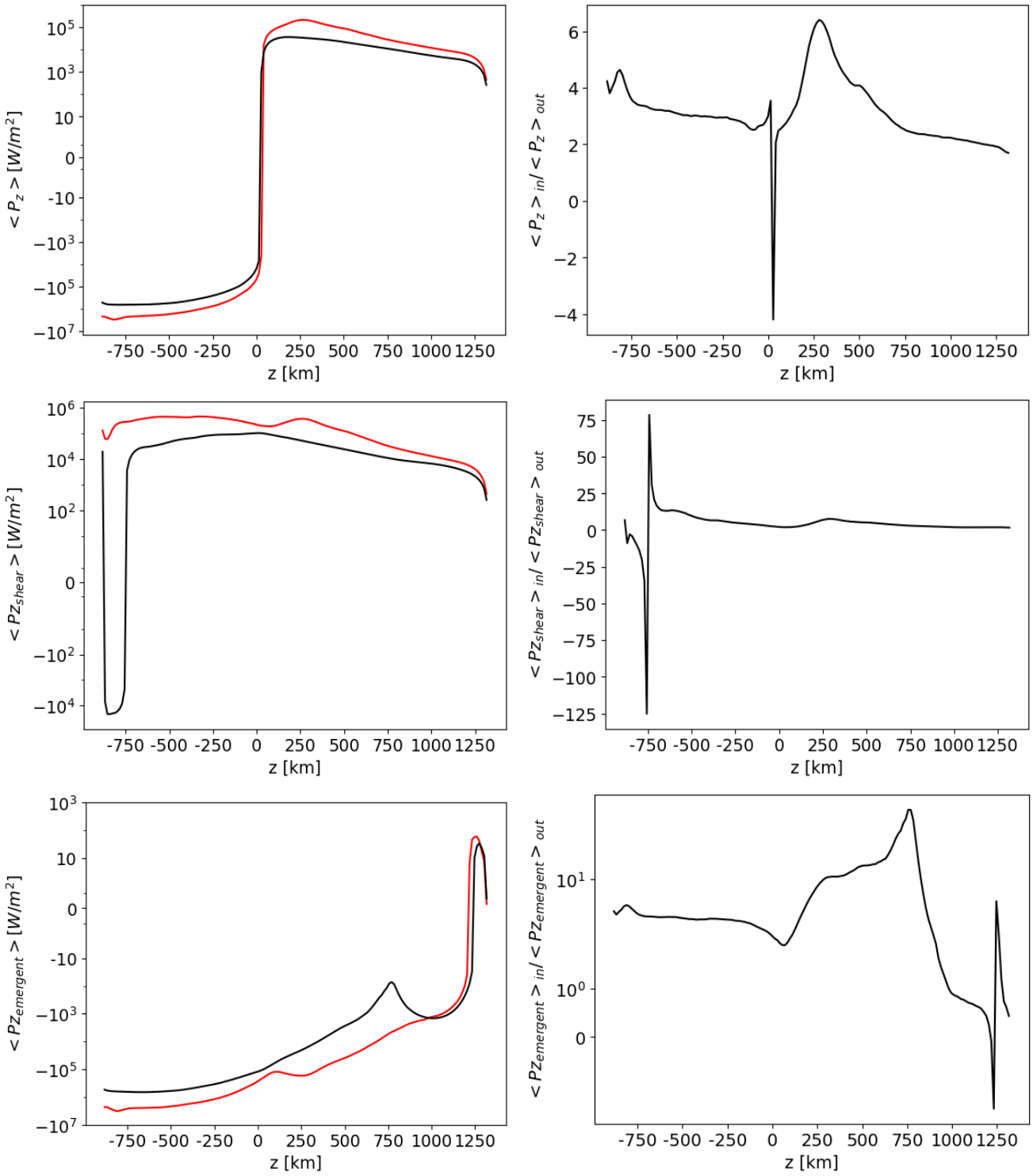

Figure 4.6: Same calculations presented in Fig. 4.5 for the $50G$ time series.

Figures 4.5 and Fig. 4.6 illustrate these quantities in the simulated atmosphere. We performed horizontal averages to get the height-dependent functions, as well as time averages to get a general idea of what is happening throughout the time series duration. The calculations have been performed in regions where vortex flows have been identified and regions where there are no vortex flows.

As we can see, there is a general agreement between both time series on the shape of the results obtained.
Sub-photospheric heights present a negative total Poynting flux, indicating that the propagation of energy magnetic energy density is mostly downwards. In this region, the Poynting flux is dominated by the "emergent" component for both time series.
At photospheric levels, there is a swap in the direction of the propagation of the magnetic energy density. This energy starts propagating upwards to the chromosphere. The generation of the Poynting vector is dominated by the "shear" component in this region for both time series.
At chromospheric heights, the direction remains positive, so upward propagation of magnetic energy density, without a clear dominating component produces the vertical Poynting flux in the $Dynamo$ time series, but for $50G$ the "shear" component remains dominant like in photospheric heights.

In more detail, we see that the "shear" component is more important in vortex flows at all heights for both time series. This result makes sense since most of the vortex flows are motions around magnetic flux concentrations. The "emergent" component, on the other hand, is mainly created by non-vortex regions in layers below the chromosphere. The chromosphere and higher layers, it is dominated by vortex flows. This is expected, since this component as said before, represents the horizontal magnetic field perturbations carried by vertical plasma motions. In subphotospheric layers, convection is the main mechanism for plasma motions, and vortex flows form at the edges of the convection channels.

Finally, we can conclude that vortex flows dominate in the generation of Poynting flux. By the sign of the curves shown at the right panels of the Figs. 4.5 and 4.6 we can determine if vortex flows and non-vortex flows contain vertical Poynting flux vectors with the same directions or opposed. But in general, vortex flows are better carriers of electromagnetic energy than the non-vortex regions, and depending on the layer this energy propagates in different directions vertically.

4.2.2 Kinetic energy density

The other quantity of interest for this work is the kinetic energy density, which can be split into vertical and horizontal components:

$$KE = \frac{1}{2}\rho \boldsymbol{v}^2$$
$$KE_z = \frac{1}{2}\rho v_z^2$$
$$KE_h = \frac{1}{2}\rho (v_x^2 + v_y^2)$$

where ρ is the mass density, and $\boldsymbol{v}$ is the velocity field with components $\boldsymbol{v} = (v_x, v_y, v_z)$.

Figures 4.7 and 4.8 represent the averaged (horizontally and temporally) kinetic energy density, and its components, as functions of height for both time series. As in the previous section, we discriminate between vortex and non-vortex regions.

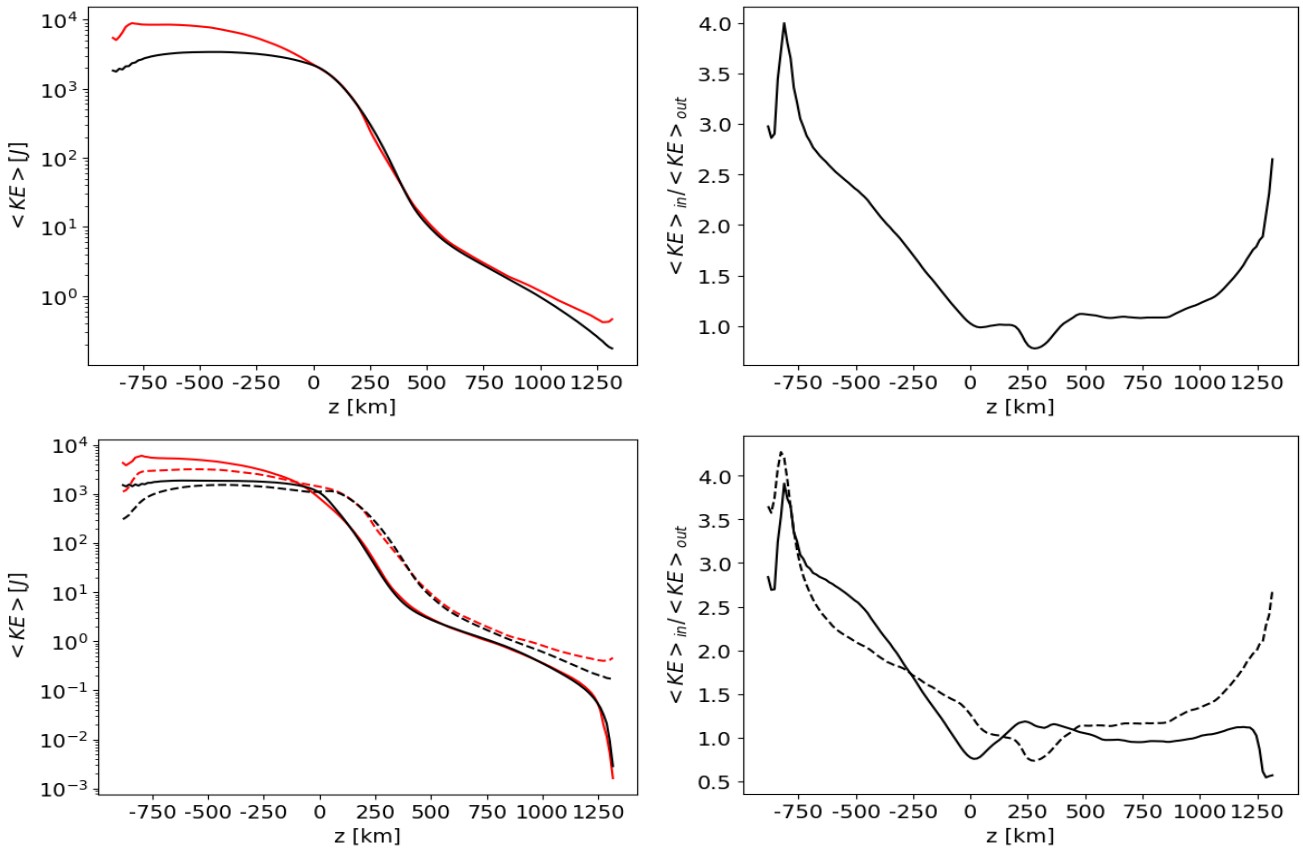

Figure 4.7: Horizontally and temporal averaged kinetic energy density as a function of height for $Dynamo$ simulation. Left panels : results for regions identified as vortex flows (red) and non-vortex regions (black). Right panels: Ratio between "inside" of vortices and "outside" of vortices. Top panels: Total kinetic energy density. Bottom panels: Vertical (solid lines) and horizontal (dashed lines) components of the kinetic energy.

As for the Poynting vector calculations, the results are similar for both time series. Vortex flows dominate the transport of kinetic energy, both vertical and horizontal, at the solar interior and the upper photosphere and higher layers. In contrast, non-vortex flows are the main contributors to the transport of kinetic energy in the low and middle photosphere. This result is expected since in these layers the generation of vorticity decreases significantly (see figure 4.3). A low number of vortex flows are identified, making their contribution very low.

In Figures 4.7 and 4.8, we can also see that vertical kinetic energy is the main contributor in subphotospheric layers, indicating that even with vortex flows the vertical velocities are quite important, expected since convection is present. From the photosphere to the higher layers the horizontal components takes the primary role in the transport of kinetic energy, indicating that horizontal velocities are more important.
At the solar interior, we can determine that vortex flows are a good mechanism for transporting kinetic energy density from the interior to the photosphere. In the solar atmosphere, the vortex flows are slightly more efficient than non-vortex regions transporting kinetic energy.

In summary, we have determined that vortex flows are a good mechanism for the transport of kinetic and electromagnetic energies since almost in all the layers from the simulation the values of the energies inside vortex channels

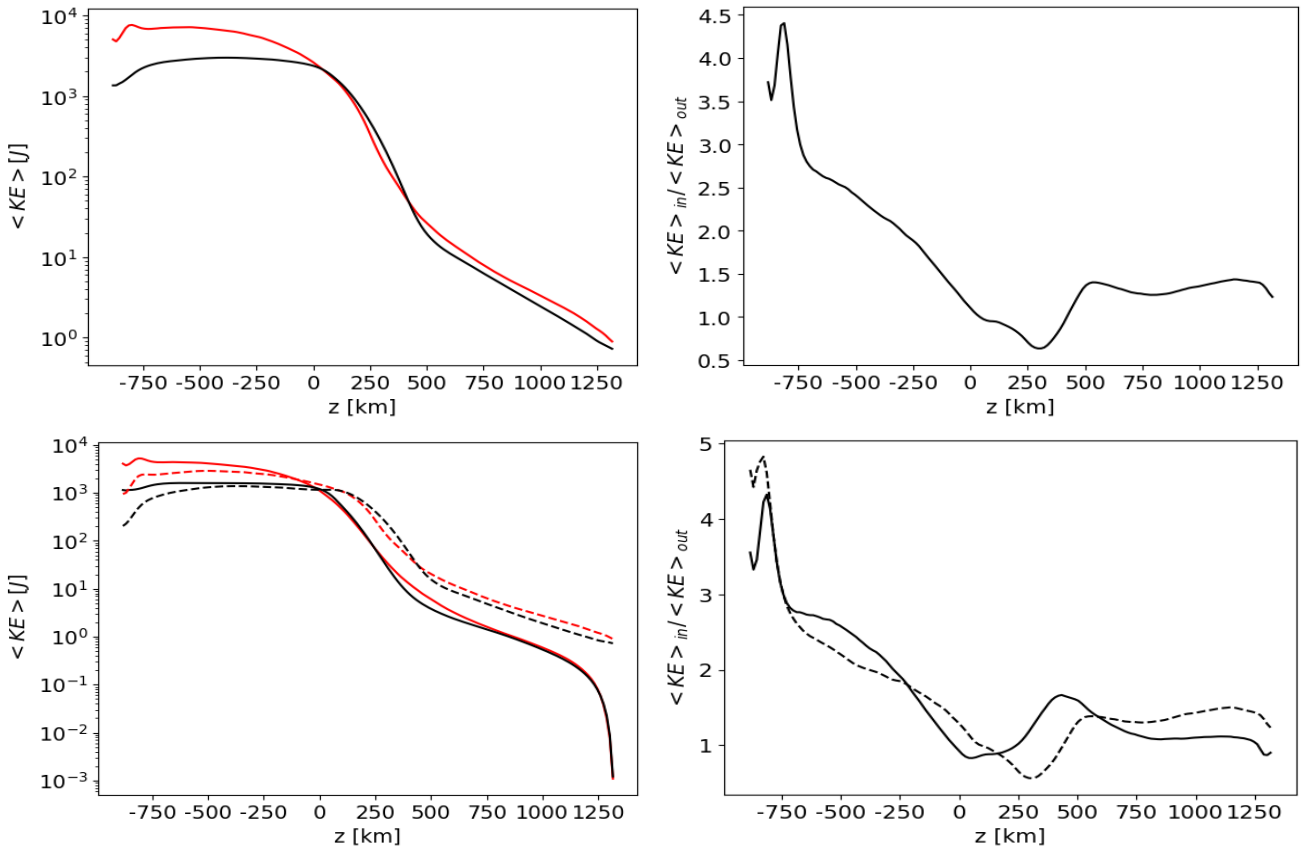

Figure 4.8: Same figure as Fig 4.7 but for the $50G$ time series.

dominate over those outside.

4.2.3 Correlation between vortices and temperature

Finally, we will study the correlation between swirling strength and the temperature distributions at different heights of interest from the simulation, the solar interior, the photosphere, and the low chromosphere, where physical conditions vary greatly.

Figure 4.9 shows 2D histograms of swirling strength and temperature for different layers of interest, for both time series. In the solar interior (lower panels), both time series present similar histograms, without an obvious correlation between the temperature and the swirling strength.

In the photosphere, we see that, for both time series, high temperatures only correspond to low swirling strength points. Most of the vortices of all strength occurs in the low-temperature regions. From here we determine that vortex flows are mainly associated with temperatures close to $6000K$, and very slowly rotating vortex flows can be paired with high temperatures.

Finally, in the chromosphere we can see a change of the trend, similar to the results in Moll et al. (2012) (see their Fig. 12). We see that vortices in the whole range of swirling strength occur in the high temperature regions. In the lower-temperature regions we observe mostly slow-rotating vortices.

In the chromosphere temperature correlates with swirling strength. In the photosphere, there is an inverse correlation

between both quantities. From this simple analysis, we cannot conclude if vortices are a heating mechanism. However, in the low chromosphere there is a direct correlation between fast rotating vortices and high temperatures.
We suspect this correlations are directly related to the energy transport from the photosphere to the lower chromosphere from the vortex flows, but a more detailed analysis should be performed to confirm it.

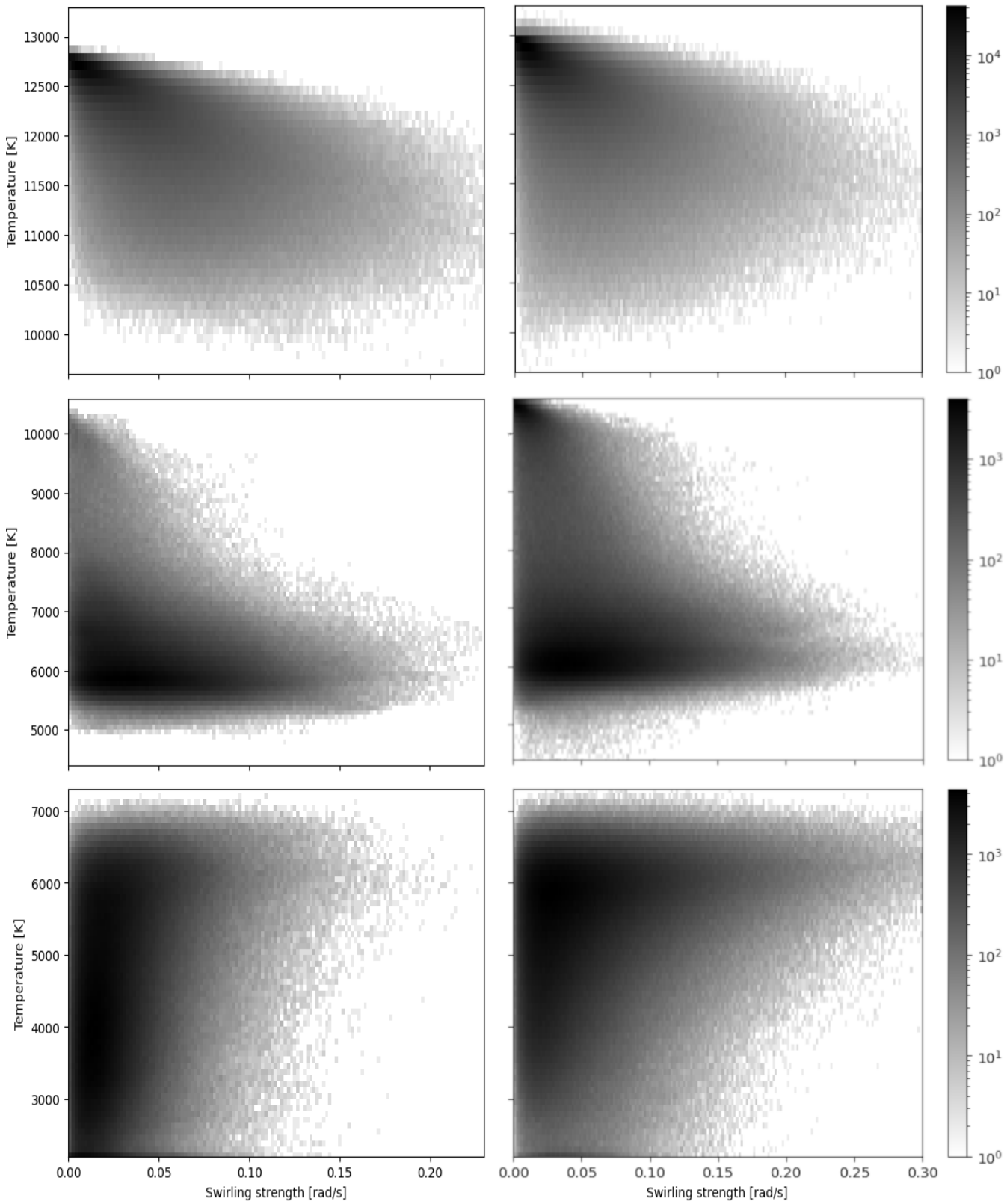

Figure 4.9: Swirling strength - Temperature 2D histograms. Left panels: $Dynamo$ simulation, Right panels: $50G$ simulation. Top panels: solar interior ($z = -532$ km), Middle panels: photosphere ($z = 28$ km), Bottom panels: chromosphere ($z = 1000$ km).

Chapter 5

Conclusions

Solar vortex flows have become a focal point of extensive research within the solar physics community. These phenomena have emerged as promising mechanisms for the transportation of kinetic and magnetic energy, directing the intricate interplay between the solar interior, photosphere, chromosphere, and corona. Moreover, scientists are delving into their potential as potent agents of solar heating.

In this work, we studied vortex flows by employing realistic simulations of the solar interior and atmosphere. Two simulations were used, each distinguished solely by the initial magnetic field configuration. The first simulation, called $Dynamo$, showcased a dynamic magnetic field configuration generated by local dynamo effects, while the second simulation, $50G$, featured an imposed initial vertical magnetic field with a flux intensity of 50G. These contrasting configurations would yield divergent outcomes in our characterization and analysis of vortex flows.

Our methodology was based on a parameter known as swirling strength. It uses eigenanalysis of the velocity gradient tensor to discern vortices. To enhance the precision of our identification mechanism, we incorporated the enhanced swirling strength criteria, as indicated in sections 3.3 and 3.4. These criteria lead us to pinpoint vortex flows within our simulation domains for both time series. Though as we remarked the identification of vortex flows is higly dependant on the criteria used. We recommend as a continuation for this work, performing a similar analysis for similar time series using different spatial resolutions. In addition, as pointed out by recent works (Canivete Cuissa & Steiner (2022)), using the Rortex or Liutex criteria that may be better for the identification of vortices, but it is still debatable.

Using Equation 3.3, we unveiled the nature of vortex flows manifesting at various heights within our simulations. Figure 3.1 shows the dynamic interplay between different vorticity components, showcasing their dependence on the initial magnetic field configuration. In the solar interior, hydrodynamic effects dominate over the generation of vortex flows, with convection emerging as the predominant mechanism. As we ascended from the photosphere to the upper chromosphere, magnetic forces assumed dominance. However, in the "Dynamo" simulation, hydrodynamic effects retained their relevance, intertwining with magnetic processes.

These results translate into what we see in Figure 4.4, showcasing the 3D structure of vortex flows. Deep within the solar interior, "Dynamo" was mostly covered by small to medium-sized vortex flows, characterized by their pronounced tilting away from the vertical axis. "50G" yielded a similar abundance of small-sized vortex flows, similar to those observed in the "Dynamo" simulation. Given that both time series shared a common hydrodynamic process for the generation

vorticity in this layer, the result was expected.

A void in vortex flow presence became evident in the photosphere, where the convergence of a sup-photospheric vortex flow and a magnetic flux footprint was required for vortex generation. This criterion proved to be more strict in the "Dynamo" simulation compared to the "50G" simulation, resulting in a noticeable reduction in vortex flows.

However, it was within the chromosphere that the true differences between the two-time series revealed themselves. "Dynamo" predominantly showcased small-sized vortex flows with irregular shapes. While a few medium-sized vortex flows did connect with the photosphere, as revealed in Figure 4.4, they remained a minority. On the other hand, "50G" gave rise to an abundance of vertically aligned, medium to large-sized vortex flows, seamlessly coiling around magnetic flux tubes. Magnetic processes primarily fueled the generation of these vortex flows, and their remarkable ability to bridge the photosphere and chromosphere became evident.

Turning our attention to Figure 4.3, we can see how much do vortex flows actually cover in our simulations as a function of height. Vortex flows spanned between 2.5% to 15% of the total area, their coverage varying with height.
In the convection zone, both time series yielded similar results, with an area coverage ranging from 7.5% to 10%.
In the photosphere a noticeable decline in area coverage due to the scarcity of vortex flows is clear, reducing to values between 2.5% and 5%.
As we moved to the chromosphere, the time series diverged once more. "Dynamo" reached its peak area coverage at approximately 600 km above the solar surface, nearly touching 15% before rapidly descending to photospheric levels at higher atmospheric layers. "50G," on the other hand, boasted its maximum area coverage of around 700 km, covering approximately 15% of the surface area, and maintained a relatively constant coverage as we ascended through the solar atmosphere.

Additionally, we delved into the ability of these vortex flows to serve as conduits for mass and energy. Our investigation focused on the height-dependent kinetic energy density and the vertical Poynting vector, contrasting regions identified as vortex flows against those that were not. We performed a decomposition of these magnitudes into their components, to check for more detailed information.

Our findings showcased the dominance of vortex flows in terms of kinetic energy density and vertical Poynting flux within the solar atmosphere, unequivocally corroborating their role as efficient propagators of mass and energy. Even so, we must remark that in the solar interior convection dominates, serving as the primary mechanism for mass and energy transportation.

Lastly, inspired by the proposition of vortex flows as potential sources of solar heating, we performed a simple analysis to check the correlation between high swirling strength and temperature, akin to the work of Moll et al. (2012).
In Figure 4.9 we can see 2D Temperature-Swirling strength histograms for different regions. Within the solar interior (z=-532 km), we observed that there is no evident correlation between these two magnitudes.

In the photosphere (z=28 km), high temperatures were confined to regions characterized by low swirling strength, while areas with lower temperatures spanned a wide range of swirling strength values. Notably, regions with high swirling strength primarily encompassed temperatures around 6000 K.

As we ascended to the chromosphere (z=1000 km), the relationship between temperature and swirling strength witnessed a remarkable reversal. Low-temperature regions correlated with low swirling strength, while high-temperature regions emerged across the entire spectrum of swirling strength. Fast swirling motions in the chromosphere exhibited a direct correlation with elevated temperatures. To determine if this vortical structures can be heating mechanism we suggest, as a continuation to this work, to study the different heating mechanism in the vortices and compare the results with regions without them. This would allow to check if vortices can be mechanism for the deposit or dissipation of energy.

In conclusion, our study has focused on the study of solar vortex flows through realistic simulations and their analysis. We have shown their diverse manifestations across different solar regions and also got insights into their roles as conveyors of mass and energy. More work needs to be done since many questions remain open but we think our findings provide a solid foundation for future explorations into the mechanisms governing the dynamics and heating of the solar atmosphere.

Bibliography

Ballester, J. L., Alexeev, I., Collados, M., Downes, T., Pfaff, R. F., Gilbert, H., Khodachenko, M., Khomenko, E., Shaikhislamov, I. F., Soler, R., Vázquez-Semadeni, E., Zaqarashvili, T. 2018, , 214(2), 58

Battaglia, A. F. 2021, *Master's thesis*

Bonet, J. A., Márquez, I., Sánchez Almeida, J., Cabello, I., Domingo, V. 2008, , 687(2), L131

Bonet, J. A., Márquez, I., Sánchez Almeida, J., Palacios, J., Martínez Pillet, V., Solanki, S. K., del Toro Iniesta, J. C., Domingo, V., Berkefeld, T., Schmidt, W., Gandorfer, A., Barthol, P., Knölker, M. 2010, , 723(2), L139

Brandt, P. N., Scharmer, G. B., Ferguson, S., Shine, R. A., Tarbell, T. D., Title, A. M. 1988, , 335(6187), 238

Canivete Cuissa, J. R., Steiner, O. 2020, , 639, A118

Canivete Cuissa, J. R., Steiner, O. 2022, , 668, A118

Chakraborty, P., Balachandar, S., Adrian, R. J. 2005, Journal of Fluid Mechanics, 535, 189

Chong, M. S., Perry, A. E., Cantwell, B. J. 1990, Physics of Fluids A, 2(5), 765

González-Morales, P. A., Khomenko, E., Downes, T. P., de Vicente, A. 2018, , 615, A67

Kato, Y., Wedemeyer, S. 2017, , 601, A135

Khomenko, E., Collados, M. 2012, in T. R. Rimmele, A. Tritschler, F. Wöger, M. Collados Vera, H. Socas-Navarro, R. Schlichenmaier, M. Carlsson, T. Berger, A. Cadavid, P. R. Gilbert, P. R. Goode, M. Knölker (eds.), Second ATST-EAST Meeting: Magnetic Fields from the Photosphere to the Corona., Vol. 463 of *Astronomical Society of the Pacific Conference Series*, 281

Khomenko, E., Collados, M., Vitas, N., González-Morales, P. A. 2021, Philosophical Transactions of the Royal Society of London Series A, 379(2190), 20200176

Khomenko, E., Díaz, A., de Vicente, A., Collados, M., Luna, M. 2014, , 565, A45

Khomenko, E., Vitas, N., Collados, M., de Vicente, A. 2018, , 618, A87

Moll, R., Cameron, R. H., Schüssler, M. 2011, The Astrophysical Journal, 533, A126

Moll, R., Cameron, R. H., Schüssler, M. 2012, , 541, A68

Nordlund, A. 1985, , 100, 209

Shelyag, S., Keys, P., Mathioudakis, M., Keenan, F. P. 2011, , 526, A5

Shelyag, S., Mathioudakis, M., Keenan, F. P. 2012, , 753(1), L22

Stein, R. F., Nordlund, Å. 1998, , 499(2), 914

Tziotziou, K., Scullion, E., Shelyag, S., Steiner, O., Khomenko, E., Tsiropoula, G., Canivete Cuissa, J. R., Wedemeyer, S., Kontogiannis, I., Yadav, N., Kitiashvili, I. N., Skirvin, S. J., Dakanalis, I., Kosovichev, A. G., Fedun, V. 2023, , 219(1), 1

Wedemeyer, S., Steiner, O. 2014, , 66, S10

Wedemeyer-Böhm, S., Rouppe van der Voort, L. 2009, , 507(1), L9

Wedemeyer-Böhm, S., Scullion, E., Steiner, O., Rouppe van der Voort, L., de La Cruz Rodriguez, J., Fedun, V., Erdélyi, R. 2012, , 486(7404), 505

Yadav, N., Cameron, R. H., Solanki, S. K. 2021, Astronomy & Astrophysics, 645, A3

Zhou, J., Adrian, R. J., Balachandar, S., Kendall, T. M. 1999, Journal of Fluid Mechanics, 387(1), 353